

## **A collinear self-emission and laser-backlighting imaging diagnostic**

S. C. Bott, G. Collins IV, K. Gunasekera, D. Mariscal, F. N. Beg, D. M. Haas, F. Veloso, I. C. Blesener, A. D. Cahill, C. L. Hoyt, B. R. Kusse, and D. A. Hammer

Citation: [Review of Scientific Instruments](#) **83**, 083507 (2012); doi: 10.1063/1.4746996

View online: <http://dx.doi.org/10.1063/1.4746996>

View Table of Contents: <http://scitation.aip.org/content/aip/journal/rsi/83/8?ver=pdfcov>

Published by the [AIP Publishing](#)

---

### **Articles you may be interested in**

[Technical overview of the millimeter-wave imaging reflectometer on the DIII-D tokamak \(invited\)a\)](#)  
Rev. Sci. Instrum. **85**, 11D702 (2014); 10.1063/1.4889735

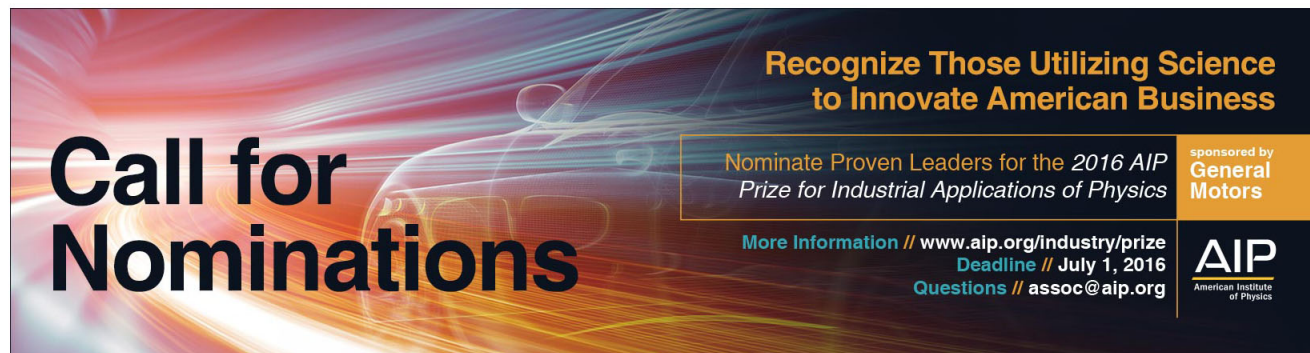
[A torquing shearing interferometer for cylindrical wire array experimentsa\)](#)  
Rev. Sci. Instrum. **79**, 10E716 (2008); 10.1063/1.2965008

[Multilayer mirror monochromatic self-emission x-ray imaging on the Z accelerator](#)  
Rev. Sci. Instrum. **77**, 10E316 (2006); 10.1063/1.2220071

[Generation of speckle-reduced phase images from three complex parts for synthetic aperture radar interferometry](#)  
Appl. Phys. Lett. **88**, 114106 (2006); 10.1063/1.2185250

[Production of ultracollimated bunches of multi-MeV electrons by 35 fs laser pulses propagating in exploding-foil plasmas](#)  
Phys. Plasmas **9**, 3655 (2002); 10.1063/1.1498116

---



**Call for Nominations**

**Recognize Those Utilizing Science to Innovate American Business**

Nominate Proven Leaders for the 2016 AIP Prize for Industrial Applications of Physics

More Information // [www.aip.org/industry/prize](http://www.aip.org/industry/prize)  
Deadline // July 1, 2016  
Questions // [assoc@aip.org](mailto:assoc@aip.org)

sponsored by  
**General Motors**

**AIP**  
American Institute of Physics

## A collinear self-emission and laser-backlighting imaging diagnostic

S. C. Bott,<sup>1,a)</sup> G. Collins IV,<sup>1</sup> K. Gunasekera,<sup>1</sup> D. Mariscal,<sup>1</sup> F. N. Beg,<sup>1</sup> D. M. Haas,<sup>2</sup> F. Veloso,<sup>3,b)</sup> I. C. Blesener,<sup>4</sup> A. D. Cahill,<sup>4</sup> C. L. Hoyt,<sup>4</sup> B. R. Kusse,<sup>4</sup> and D. A. Hammer<sup>4</sup>

<sup>1</sup>University of California San Diego, La Jolla, California 92093-0417, USA

<sup>2</sup>General Atomics, San Diego, California 92121, USA

<sup>3</sup>Comision Chilena de Energia Nuclear, Casilla 188-D, Santiago, Chile

<sup>4</sup>Laboratory for Plasma Studies, Cornell University, Ithaca, New York 14850, USA

(Received 10 June 2012; accepted 5 August 2012; published online 23 August 2012)

In this work we demonstrate a design for obtaining laser backlighting (e.g., interferometry) and time-resolved extreme ultraviolet self-emission images along the same line-of-sight. This is achieved by modifying a single optical component in the laser collection optics with apertures and pinhole arrangements suitable for single or multiple frame imaging onto a gated detector, such as a microchannel plate. Test results for exploding wire experiments show that machining of the optic does not affect the overall quality of the recovered laser images, and that, even with a multiple frame system, the area sacrificed to achieve collinear imaging is relatively small. The diagnostics can therefore allow direct correlation of laser and self-emission images and their derived quantities, such as electron density in the case of interferometry. Simple methods of image correlation are also demonstrated.

© 2012 American Institute of Physics. [<http://dx.doi.org/10.1063/1.4746996>]

### I. INTRODUCTION

In a range of plasma experiments one wishes to examine several details of the system as a function of time to better understand how various details are interconnected, and hence more fully understand the dominant physics processes at work. Determination of the plasma density and temperature are at the core of such studies. For plasmas of moderate densities ( $10^{16}$ - $10^{19}$  cm<sup>-3</sup>) laser-based interferometry is a common tool to determine electron densities given the relative ease of setup and data analysis to recover two-dimensional (areal) electron density maps, or by use of Abel-inversion techniques, three-dimensional interpretations. If determination of plasma temperature is required simultaneously, a self-emission or spectroscopic diagnostic is typically set up in tandem with interferometry to observe in a suitable energy range. It is often desirable to recover density and temperature information along the same line-of-sight to enable an exact correlation of the two, which then allows a good comparison to theoretical or computational work. In practice this can be problematic, given the different collection requirements for the two diagnostics, and these are commonly set up on different vacuum ports at different viewing angles to the experiment. This makes a direct comparison of these two types of data difficult without making some perhaps significant assumptions about the plasma geometry.

For imaging interferometry, a parallel optical-laser beam is used as the object arm of a Mach-Zehnder or other interferometer design, whilst emission may be collected as a pinhole or slit image. For relatively cool plasmas emitting in the optical range, the collection of all light along one line of sight followed by isolation of the laser image by notch filter may be possible. However, for wavelengths shorter than the

visible such methods become complex and expensive in the extreme ultraviolet (XUV) and x-ray range ( $h\nu > 5\text{eV}$ ). In this work, we demonstrate a new collinear interferometry and gated emission imaging diagnostic which can be accurately correlated to address such issues.

The concept is very simple, and shown schematically in Figure 1, and experimentally in Figure 2. A reflection optic is mounted in front of the emission image detector to transport a parallel laser beam out to further collection optics. In this optic, a small hole is drilled to allow radiation to pass through unaffected to a pinhole mounted at the rear surface. This projects an image onto the emission detector in the normal way, whilst the reflection optic absorbs or reflects all other radiation. Both the laser image and the self-emission image are then recovered along the same line-of-sight, and, by suitable gating, at the same time during an experiment. The hole in the reflecting optic need only be a small portion of the total surface area, and does not affect the ability to compare the images away from this region. Since this is essentially a single optic mounted along one line of sight, if it is mounted in a separate vacuum sealable chamber, it can be easily transported as a unit from experiment to experiment, requiring only relatively simple realignment of existing setups to be used. This also frees up other vacuum ports for additional diagnostics, or multiple lines of sight for multiple collinear setups, which is often a significant advantage for small experiments.

### II. DESIGN AND CONSTRUCTION

The principle design issues are the machining of the reflective optic to allow pinhole imaging, and effects of this on the quality of the reflected beam. Initial drilling tests used 1" diameter mirrors which were  $\sim 3\text{-}5$  mm thick. Drilling with diamond-tipped bits was successful, but the need to machine at 45 degrees and to achieve a uniform channel over several millimetres was problematic. A simple perpendicular drilling

a)Electronic mail: sbott@ucsd.edu.

b)Present address: Departamento de Fisica, Pontificia Universidad Catolica de Chile, Av Vicuna Mackenna 4860, Macul, Santiago, Chile.

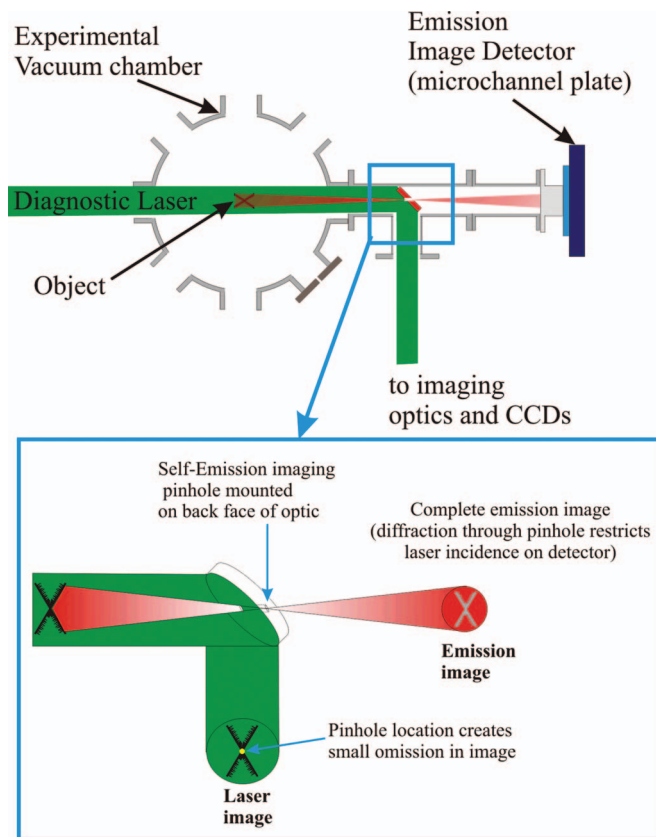


FIG. 1. Conceptual design of the collinear diagnostic.

process was adopted for these early tests (Sec. III), and the optic was switched to economic visible light beamsplitters (50% reflection - Thorlabs EBS2) which are only 1 mm thick. This proved successful and easy to achieve a clean hole with a simple drill bit. The use of a beamsplitter necessitates a beam block for the transmitted portion of the laser and other emission, but this is simply accomplished using a cardboard or metal backing to the beamsplitter which can be separately constructed. It should be noted that drilling at 45 degrees is preferable since the hole may be smaller (i.e., affect a smaller area of the reflecting surface – Sec. IV). The most effective solution is with hollow end mill bits which provide a clean drill at the front surface if machined sufficiently slowly. The beamsplitter is mounted onto a brass backing plate to limit fracture on breakout at the reverse surface, but generally this will not affect use of the optic provided the front reflecting surface is maintained.

The limits of the emission imaging are those of a pinhole camera, and Eqs. (1) and (2) can be used to determine the spatial (geometric) resolution (Eq. (1)) of an image which passes energies above a lower diffraction limit (Eq. (2))

$$L_{geo} = d \left( 1 + \frac{p}{q} \right), \quad (1)$$

$$L_{diff} = 1.22 \frac{\lambda p}{d}, \quad (2)$$

where  $d$  is the pinhole diameter,  $p$  is the object-pinhole distance, and  $q$  is the pinhole camera distance. Generally  $L_{geo}$  is calculated from the experimental setup, and then  $L_{diff}$  is set to  $L_{geo}$  to calculate the upper wavelength limit  $\lambda$  (lower energy limit) of radiation focused through the pinhole. Initial tests used a pinhole mounted directly onto the rear of the beamsplitter and at 45 degrees to the experiment. From Eqs. (1) and (2), this will affect the spatial and spectral information along both axes, since these rely on the pinhole dimension, which is an ellipse when viewed from the experiment due to the pinhole tilt. To avoid this, pinholes in later designs are mounted perpendicular to the experiments (i.e., as for typical pinhole imaging) to allow a simple analysis of the images (see Sec. IV). For these initial tests, however this was not completed.

There were initial concerns about the stresses placed on the optic during a lengthy drilling process, and how this might affect the reflected beam. To assess this, a drilled beamsplitter was used to set up an interferometer using the arrangement in Fig. 1. Figure 3 shows an image of a wire array driven by the 250 kA, 150 ns GenASIS machine<sup>1</sup> at UC San Diego. The diagnostic laser is a frequency doubled Nd:YAG with a pulse duration of 5 ns, and the image is taken at peak current.

The location of the pinhole in both the pre-experiment and experiment images can be clearly seen in the interference pattern. It is not possible to infer reliable electron densities in this region, but the image masking routines available in the IDEA software<sup>2</sup> used for this analysis allow areas away from this to be analysed without including this region. IDEA uses a two-dimensional spatial fast Fourier transform to isolate the carrier frequency and compare the experimental image with an image taken before the experiment where no plasma is present (for a full discussion of the routines available in the IDEA software, refer to Hipp *et al.*<sup>3</sup>). The phase shift  $\Delta\phi$  induced by the plasma is proportional to the change in refractive index along the integrated line of sight and depends on the laser frequency  $\omega$ , the critical density in the plasma

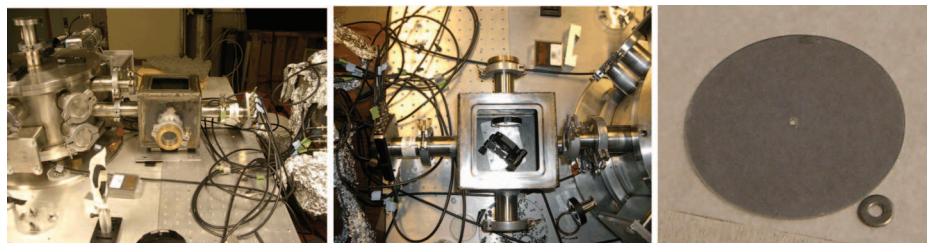


FIG. 2. Mounting arrangement on the GenASIS pulser<sup>1</sup> at UC San Diego: Photographs of (left) side and (center) top view of mounting of collinear diagnostic in vacuum chamber and (right) photograph of beamsplitter drilled with 1.6 mm hole used for proof-of-principle experiments.



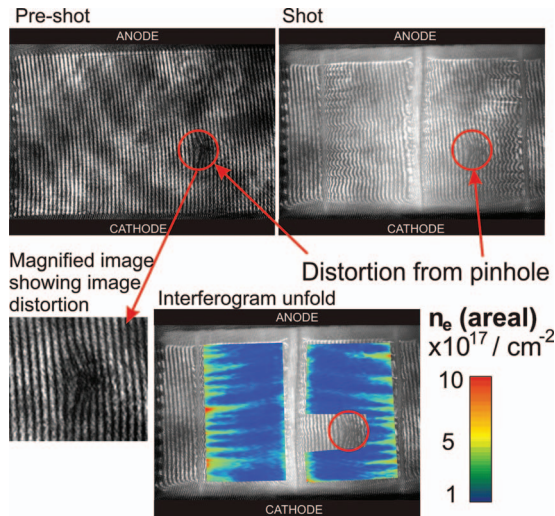


FIG. 3.  $4 \times 10 \mu\text{m}$  Cu wire array on the 250 kA GenASIS machine<sup>1</sup> at UC San Diego demonstrating that the effect of the pinhole drilled into the optic is clearly observable (circled in each image), but limited to a small region of the optic.

$n_c = \omega^2 m \epsilon_0 / e^2$ ,<sup>4</sup> and the plasma density

$$\Delta\phi = \frac{-\omega}{2cn_c} \int n_e dl. \quad (3)$$

For a laser wavelength of 532 nm, Eq. (1) can be simplified to

$$\int n_e dl = 4.2 \times 10^{17} f. \quad (4)$$

The fringe shift in the experimental image,  $f$ , can then be plotted as a function of space and converted to areal (i.e., integrated along the line of sight of the diagnostic) electron density through Eq. (2). This analysis routine relies on the accuracy to which the fringes can be resolved and compared between experiment and pre-experiment images, and errors are typically quoted at  $\sim 1/4$  fringe shift, or  $n_{e,\text{areal}} \sim 1 \times 10^{17} \text{ cm}^{-2}$ . The recovered densities and features are in line with those expected for this experiment (e.g., Ref. 5) and the machining of the beamsplitter does not appear to affect the imaging in any significant way.

### III. PROOF-OF-PRINCIPLE EXPERIMENTS

Initial testing to demonstrate proof-of-principle of the combined diagnostic was performed at UC San Diego. The experiments again used the GenASIS machine as for images in Figure 3, but used a single central wire in order to maximise the XUV emission used to form the self-emission image on the microchannel plate (MCP). In order to provide sufficient flux, a pinhole diameter of  $600 \mu\text{m}$  was used at a magnification of 0.9 and imaged onto one quadrant of an MCP with a 5 ns gate time. This combination passes radiation with energies greater than  $\sim 1 \text{ eV}$ . The laser pulse length was again 5 ns as above. By co-timing the diagnostics, an image of the single wire explosion was obtained at 65 ns into the current drive simultaneously on both diagnostics (Figure 4). The recovery of these images demonstrates the principle of the diagnostic for experiments. However, several improvements are

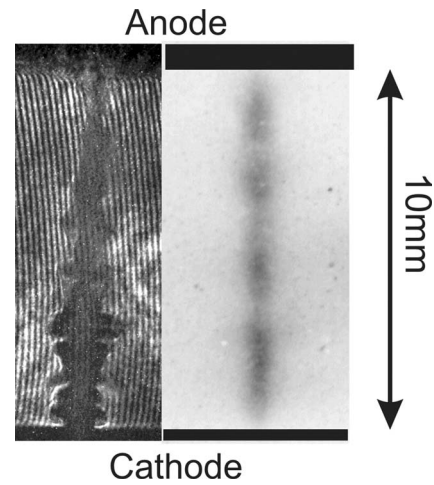


FIG. 4. Images of a single wire explosion imaged simultaneously (65 ns) and collinearly: (left) an interferogram and (right) a gated XUV self-emission image.

desirable. The use of large pinholes and moderate magnification means the spatial resolution of the self-emission image is  $\sim 1.3 \text{ mm}$ , which compares rather poorly with that of the laser image of  $< 50 \mu\text{m}$  (e.g., Ref. 6). Similarly the use of single wires to give large XUV flux means that areas where the interferogram is useful are limited to very strong density gradients at the plasma edge, before light is refracted out of the collection optics. Due to the difference in spatial resolution it is very difficult to compare the images in anything but very simplistic terms, and even the connection to the electrodes in the self-emission image can be problematic.

### IV. MULTIPLE PINHOLE DESIGN AND IMPLEMENTATION

A second series of experiments was carried out at Cornell University that incorporated many of the modifications suggested by the above results. A 4-strip MCP camera was to be used and a 4-pinhole design was constructed to image one pinhole onto each strip of the camera. The design, shown in Figure 5, uses recessed mounts for the pinholes to enable imaging perpendicular to the load, and hence obtain the same spatial and energy resolution in both the axial and radial planes. The mounts are essentially cylinders truncated at the appropriate angle and then inserted and soldered into the brass backing plate, which also served to prevent unwanted light reaching the MCP camera. It should be noted that it is possible that laser light could be reflected from the brass backing plate, causing ghosting in the interferometry images. This was not an issue in the present setup, and could be easily remedied by using a non-reflective coating on the brass used here, or machining the backing plate from a material which can be anodized, such as aluminium.

Once completed, both the beamsplitter and the brass backing plate containing the pinhole supports are mounted into a single kinematic optics mount, and placed into a small vacuum chamber. Photographs of the completed setup are given in Figure 6. The diagnostic is aligned prior to closure of the vacuum chamber. Vacuum throughput controls were not

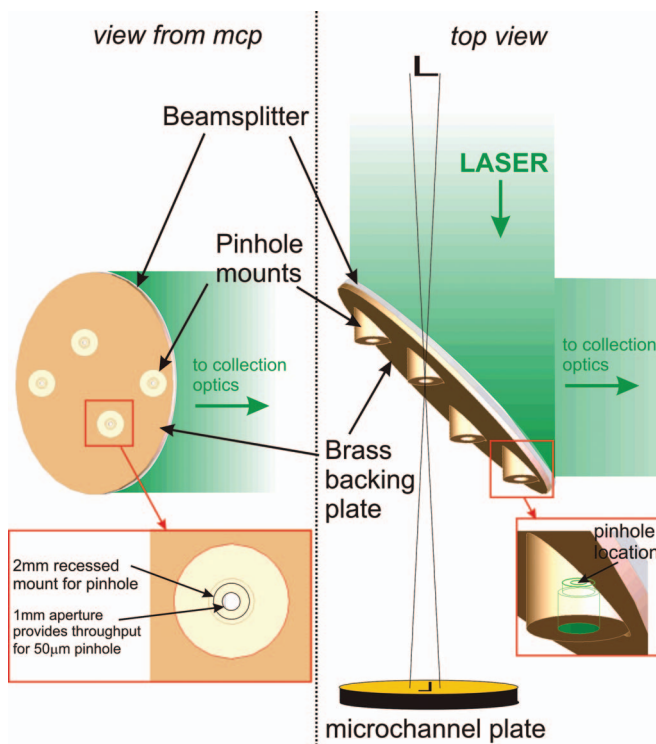


FIG. 5. Multiple pinhole setup including mounting of pinholes perpendicular to experiments.

used. However, the setup proved to be sufficiently robust to the mechanical shock of the experiments, and required little re-alignment between shots.

As an example of the capability of this diagnostic, we present results from experiments using inverse wire arrays<sup>7</sup> on the XP generator.<sup>8</sup> The generator was used in a long-pulse mode by reducing spark gap separation in the output water switches, thereby essentially bypassing the pulse-forming line and producing a current pulse with a maximum of 260 kA in a rise-time of 145 ns. Wire arrays used  $2 \times 13 \mu\text{m}$  tungsten wires on a diameter of 10 mm. The radially outwards Lorentz force accelerates plasma to supersonic velocities a short distance from the initial wire position, and this plasma flow impacts a small obstruction placed in the flow. The flow is hydrodynamic (ion mean free path  $\ll$  system size) and a bow shock is formed in the flow at the position of the obstruction. Discussion of the shock regions will be presented in a future publication; here we concentrate on the features of the flow upstream of the objects (i.e., closer to the wire). Figure 7(a) shows a schematic diagram of the experimental arrangement, along with the self-emission image (Fig. 7(b)) and laser interferometer image (Fig. 7(c)) taken at the same time in a single shot using the collinear diagnostic. Note that the plasma flow radially outwards from the wire shows non-uniformity in the axial direction, as has been noted in many previous experiments.<sup>9–12</sup> The new diagnostic allows, for the first time, a direct spatial comparison of the emission (i.e., hotter, more strongly radiating) regions with the electron density profiles. Examples of this are given in Figures 8 and 9. The laser interferogram is again analysed using the IDEA software to provide areal electron density maps.

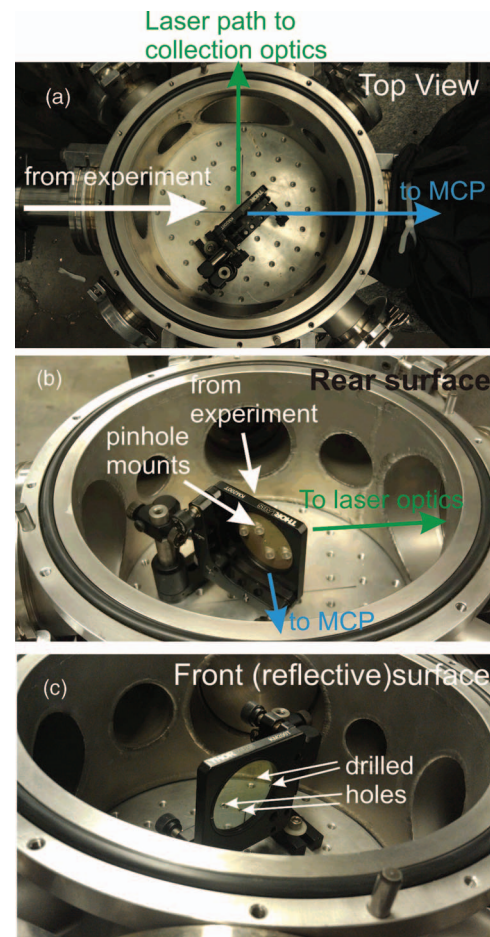


FIG. 6. Photographs of the multiple pinhole collinear diagnostic as mounted on the XP generator at Cornell University.

Figure 8(a) shows a section of the interferogram which had been analysed and overlaid on the original image. Areal electron densities are generally of order  $1 \times 10^{18} \text{ cm}^{-2}$  and the axial variation in the flow density, typically referred to as “ablation flares,” is clearly visible. Figure 8(b) shows a scaled section of the self-emission image which is vertically aligned to the laser interferogram, and a similar variation in the emission can be observed between the wire and the shocks in the flow formed at the obstructions.

The experimental set-up is sufficiently distinctive in these images that spatial correlation is possible by aligning various parts of the image (e.g., cathode post, cathode top edges, wire position, obstruction positions). Combined with the known magnifications of the images, a good correlation can be performed. The errors in this process are estimated at approximately  $\pm 100 \mu\text{m}$ , or  $\sim 0.5\%$  of the 16 mm axial region over which the two images are coincident. This is determined from tests using data from several shots, and overlaying emission and laser images. This method is rather crude, but allows alignment of regions with good confidence where spatial scales of interest are of order 0.5 mm or so, such as the ablation flares examined here.

From the images, lineouts of both the areal electron density and self-emission can be taken and directly compared spatially. This is shown in Figure 9. The vertical lines are correlated with the position of the “ablation flares” (i.e.,



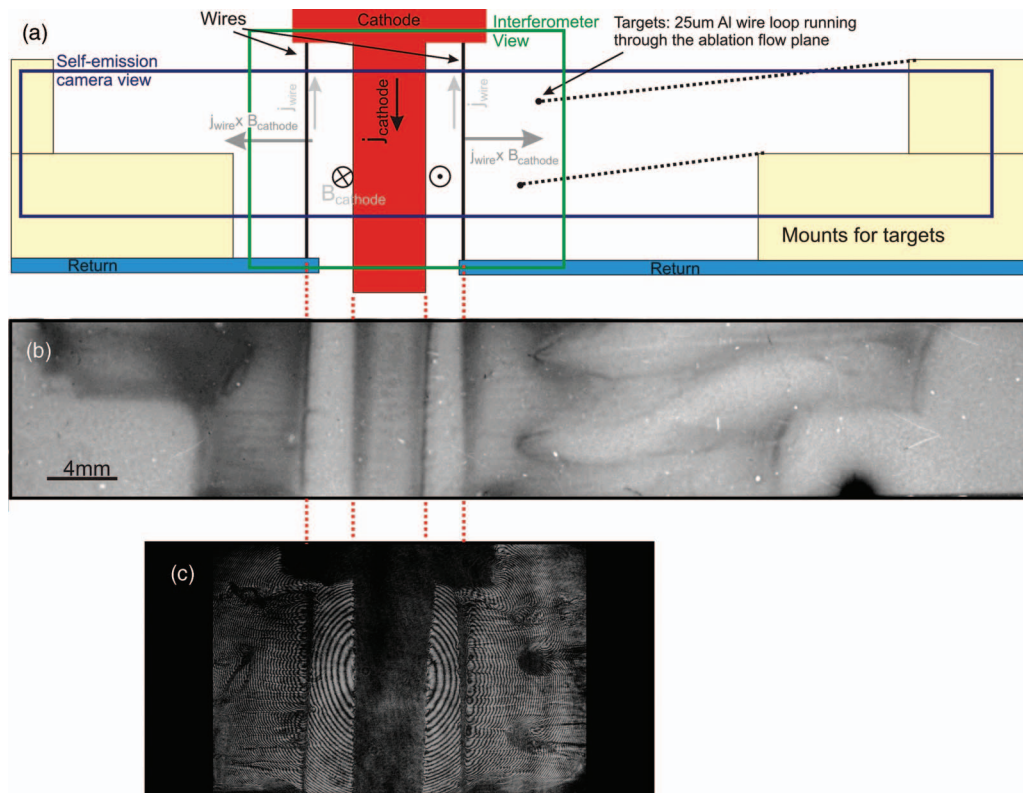


FIG. 7. (a) Schematic diagram of inverse wire array experiments on the XP generator (260 kA, 145 ns) along with (b) gated self-emission image and (c) laser interferogram taken at 158 ns using the collinear diagnostic.

high areal electron density) in the interferogram at the position of the lineout given in the plots in Fig. 9(a). The lines run through the spatially correlated interferogram image (Fig. 9(b)), self-emission image (Fig. 9(c)), and self-emission lineout (Fig. 9(c)). Note here that the laser interferogram does not include the wire itself in the analysed portion, since the electron density close to the wire is too high to follow fringes, but the emission image does include the wire; the lineouts across the images in Figure 9 are in the same spatial location in relation to the wire and hardware. Examination of the lineouts and images in this way shows that the regions of high electron density are correlated with regions of low emission in the flares. This is consistent with inferences from previous experimental studies (e.g., Ref. 13; Figure 2), but confirmed definitively for the first time with this collinear diagnostic. Further examination of this correlation and discussions of physical implications will be published elsewhere.

Whilst the methodology for correlating images is simple and effective for the types of images generated by the present studies, it is not ideal. Indeed, the need to have several points of reference in the experimental hardware limits application in systems where this is not possible. What is required to improve versatility of the method is a spatial fiducial which can be observed equally well in both types of image to be correlated. An ideal candidate is perhaps not obvious, and may depend on the exact setup and image types. Here, we demonstrate the use of a simple wire mesh which is placed on the nearside (i.e., slightly closer to the diagnostic than the experimental load). The mesh is easily imaged by the laser interferometry channel, and is backlit by the plasma emission, appearing in relief in the emission image (Figure 10).

The location of the grid from the laser image focal plane and possible ablation of the edges of the grid will affect the appearance of the grid edges, and may appear differently in

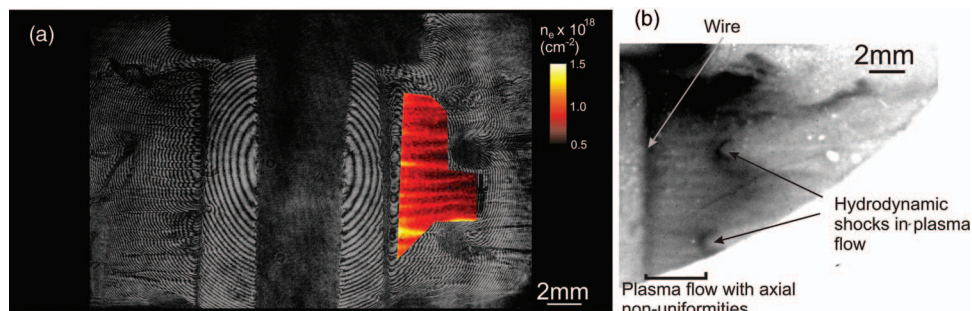


FIG. 8. (a) Interferogram from Figure 7 overlaid with section analysed for areal electron density, and (b) section of the self-emission image in Figure 7 scaled to and vertically aligned with the interferogram.

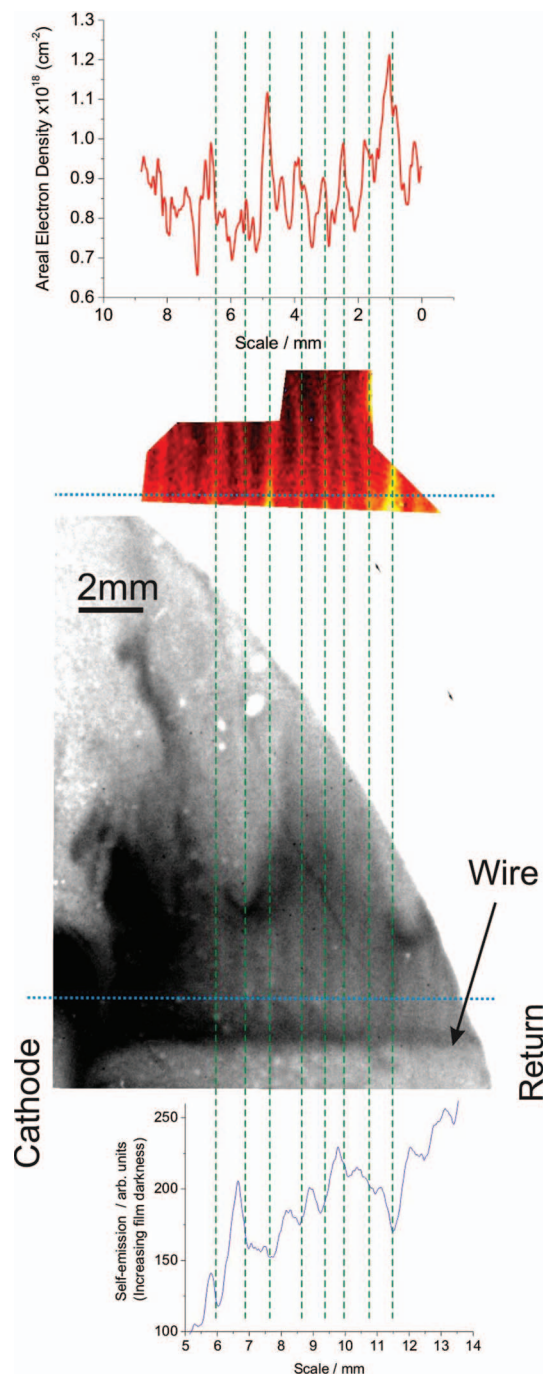


FIG. 9. Spatially correlated plots and images for (a) areal electron density lineout (blue dotted line on interferogram image), (b) analysed region of interferogram image, (c) self-emission image, and (d) lineout of self-emission taken at the same position as that for the interferogram lineout.

emission and laser images. However, correlation of several of the mesh cross-points would provide good location points for both the radial and axial spatial scales. In principle, one can simply use grids of increasingly smaller period to correlate images to better degrees. In this way, a more accurate location of images may be achieved while sacrificing some small portion of the image.

There are several important points that should be borne in mind whilst using this diagnostic arrangement. Firstly, although both the laser and emission images are collinear, this

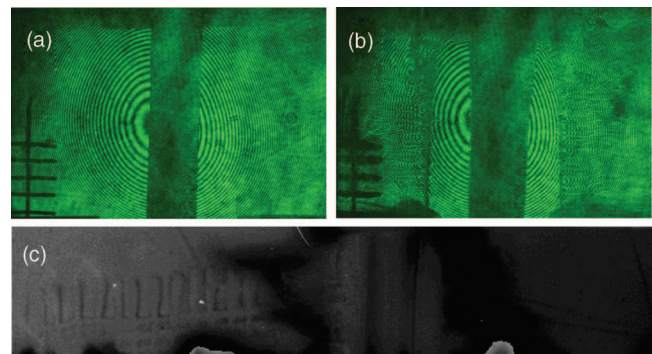


FIG. 10. Laser interferogram and self-emission images taken using the collinear diagnostic where a metallic grid was placed close to the experiment (a) pre-experiment, (b) experiment laser interferogram image, and (c) gated self-emission image from a similar shot.

is only true if a single pinhole is used (as in Sec. III) and the laser image is centred about this, as in Secs. I–III. For multiple pinholes, as used in Sec. IV, the angle subtended through the pinholes relative to the laser direction is small only when the distance of the pinhole/beamsplitter from the object is large. The smaller this distance, the larger the angular separation of the laser and pinhole emission images. For the present setup, the largest angle subtended by the multiple pinhole setup is  $\sim 1.5$  degrees, and the smallest is  $\sim 0.8$  degrees. Similarly, the 45 degree angle of the pinhole/beamsplitter means that the pinholes along this direction will be at slightly different distances from the object. For a common detector plane for the emission diagnostic, the magnification of the images from each pinhole will be slightly different, although the magnification is obviously fixed within any particular frame. Again, the larger the object- pinhole/beamsplitter distance, the less pronounced this will be. For the geometry used in Sec. IV, the difference between the smallest and largest magnification is about 10%.

The main issue in this work is the flux for the emission image. Using a more sensitive or multiple microchannel plate high gain detector would help significantly here. Alternatively, it is possible to place the pinhole/beamsplitter inside the main vacuum chamber within a few inches of the experimental load. This was briefly tested at UC San Diego, and as long as little debris is projected towards the pinhole/beamsplitter it will generally survive.

One might also imagine several variations of this diagnostic arrangement. The use of different size pinholes gated at the same time would provide some limited spectral information through the different diffraction limits. This is a commonly used method and was implemented for some of the test cases not reported here. Alternatively, one or more pinholes may be designed to project XUV emission to a spectrograph or streak camera, thereby extending the range of information along a single line-of-sight.

## ACKNOWLEDGMENTS

This work was funded through Department of Energy Contract DE-SC0006958, Department of Energy/National Science Foundation Partnership in Basic Plasma Science under Contracts DE-SC-0001992 and NSF-PHY-0903876, and

PBCT-CONICYT Chile PSD-01. Work at Cornell University was supported under the NNSA Stockpile Stewardship Academic Alliance program through DOE Cooperative Agreement DE-FC03-02NA00057. The authors are grateful to Todd Blanchard for the machining of the multiple pinhole system used in this work.

- <sup>1</sup>S. C. Bott, D. M. Haas, R. E. Madden, U. Ueda, Y. Eshaq, G. Collins IV, K. Gunasekera, D. Mariscal, J. Peebles, F. N. Beg, M. Mazarakis, K. Struve, and R. Sharpe, *Phys. Rev. ST Accel. Beams* **14**, 050401 (2011).
- <sup>2</sup>IDEA, V1.7, Graz University of Technology, Austria (<http://optics.tu-graz.ac.at>).
- <sup>3</sup>M. Hipp, J. Woisetschleager, P. Reiterer, and T. Neger, *Measurement* **36**, 53 (2004).
- <sup>4</sup>I. H. Hutchinson, *Principles of Plasma Diagnostics*, 2nd ed. (Cambridge University Press, 2002), p. 116.
- <sup>5</sup>S. C. Bott, D. M. Haas, Y. Eshaq, U. Ueda, R. E. Madden, G. W. Collins IV, and F. N. Beg, *IEEE Trans. Plasma Sci.* **38**, 567 (2010).

- <sup>6</sup>R. E. Madden, S. C. Bott, D. Haas, Y. Eshaq, U. Ueda, G. Collins, and F. N. Beg, *Phys. Plasmas* **15**, 112701 (2008).
- <sup>7</sup>A. J. Harvey-Thompson, S. V. Lebedev, S. N. Bland, J. P. Chittenden, G. N. Hall, A. Marocchino, F. Suzuki-Vidal, S. C. Bott, J. B. A. Palmer, and C. Ning, *Phys. Plasmas* **16**, 022701 (2009).
- <sup>8</sup>D. H. Kalantar, Ph.D. dissertation, Cornell University, May 1993.
- <sup>9</sup>S. V. Lebedev, F. N. Beg, S. N. Bland, J. P. Chittenden, A. E. Dangor, M. G. Haines, S. A. Pikuz, and T. A. Shelkovenko, *Phys. Rev. Lett.* **85**, 98 (2000).
- <sup>10</sup>J. P. Chittenden and C. A. Jennings, *Phys. Rev. Lett.* **101**, 055005 (2008).
- <sup>11</sup>G. W. Collins, D. Marsical, D. M. Haas, R. E. Madden, K. Gunasekara, J. Kim, M. L. L. Abarr, S. C. Bott, F. N. Beg, and J. P. Chittenden, *New J. Phys.* **14**, 043021 (2012).
- <sup>12</sup>S. C. Bott, D. M. Haas, Y. Eshaq, U. Ueda, S. V. Lebedev, J. P. Chittenden, J. B. A. Palmer, S. N. Bland, G. N. Hall, D. J. Ampleford, and F. N. Beg, *IEEE Trans. Plasma Sci.* **36**, 2759 (2008).
- <sup>13</sup>S. N. Bland, S. V. Lebedev, J. P. Chittenden, G. N. Hall, and F. Suzuki-Vidal, D. J. Ampleford, S. C. Bott, J. B. A. Palmer, S. A. Pikuz, and T. A. Shelkovenko, *Phys. Plasmas* **14**, 056315 (2007).